Title

Parametric Study of Transpiration Cooling Using Oxides for Sharp Hypersonic Leading Edges

Authors

Ko, Danny D
Mannion, Anthony
Zhong, Xiaolin
et al.

Publication Date

2024

DOI

10.2514/1.t6991

Peer reviewed

Parametric Study of Transpiration Cooling Using Oxides for Sharp Hypersonic Leading Edges

Danny D. Ko,* Anthony Mannion,† Xiaolin Zhong,‡ and Yongho Sungtaek Ju§
University of California Los Angeles, Los Angeles, California 90095

https://doi.org/10.2514/1.T6991

Recent escalating interest in the development of highly maneuverable hypersonic vehicles demands sharp leading edges. However, sharp leading edges induce severe aerothermal conditions where conventional passive or ablative thermal protection systems fail to protect the leading edge. Here, we numerically demonstrate transpiration cooling employing oxide coolants as a new alternative system to thermally protect sharp leading edges. We parametrically characterize the performance of transpiration cooling for various coolant properties, flight conditions, and leading edge radii using a semi-analytic boundary-layer model validated with third-order direct numerical simulations. We further utilize direct numerical simulation to examine the impact of the thermochemical behavior of oxide vapors with the external hypersonic flow on transpiration cooling. Our findings do not readily align with an optimal set of material properties for transpiration cooling. Instead, certain coolant properties are more appropriate for various flight conditions and leading edge sizes. Our results also demonstrate that the thermochemical interactions between the oxide vapors and the external hypersonic flow have a negligible impact on the performance of transpiration cooling. Our study provides numerical frameworks to evaluate the performance of transpiration cooling and optimize the coolant properties for various flight conditions to protect sharp leading edges, which are paramount across hypersonic applications.

Nomenclature

C	=	mass fraction
c_p	=	specific heat, $\mathrm{J}/(\mathrm{kg}\cdot\mathrm{K})$
D	=	binary or mixture diffusion coefficient, m^2/s
e	=	specific energy, J/kg
f	=	similarity stream function
h	=	specific enthalpy, J/kg
j	=	diffusive mass flux, $\mathrm{kg}/(\mathrm{m}^2\cdot\mathrm{s})$
k	=	thermal conductivity, $\mathrm{W}/(\mathrm{m}\cdot\mathrm{K})$
L	=	latent heat of evaporation, J/mol
Le	=	Lewis number, $\rho c_p D/\mu$
M	=	molar mass, kg/mol
$\dot{m}$	=	mass flux, $\mathrm{kg}/(\mathrm{m}^2\cdot\mathrm{s})$
P	=	pressure, Pa
Pr	=	Prandtl number, $c_p\mu/\mathrm{k}$
Q	=	vibrational energy source
R	=	universal gas constant, $\mathrm{J}/(\mathrm{mol}\cdot\mathrm{K})$
R_b	=	leading edge radius of curvature, m
r	=	distance from axisymmetric line to surface, m
T	=	temperature, K
u_n	=	velocity in nth direction, m/s
V	=	velocity, m/s
X	=	mole fraction
x	=	distance along surface, m
y	=	distance normal to surface, m
α	=	accommodation coefficient
ϵ	=	emissivity
θ	=	nondimensional temperature
μ	=	viscosity, $\mathrm{Pa}\cdot\mathrm{s}$
ρ	=	density, kg/m^3
ω	=	species source term

Subscripts

a	=	atomic air species
c	=	evaporating species
e	=	boundary-layer edge
eq	=	equilibrium or saturation
k	=	vaporizing species
o	=	stagnation point
s	=	surface
T	=	translational
v	=	vibrational

Received 16 January 2024; accepted for publication 18 April 2024; published online 6 June 2024.

*Ph.D. Candidate, Mechanical and Aerospace Engineering Department; dko1217@ucla.edu.

†Ph.D. Candidate, Mechanical and Aerospace Engineering Department; ajmannion@g.ucla.edu (Corresponding Author).

‡Professor, Mechanical and Aerospace Engineering Department; Associate Fellow AIAA.

§Professor, Mechanical and Aerospace Engineering Department.

I. Introduction

HYPERSONIC flight is a critical aspect of space exploration, aviation, and national security. In recent years, interests in the development of hypersonic vehicles with sharp leading edges have surged to achieve superior maneuverability and to maximize the lift-to-drag ratio. However, as the curvature of the leading edge decreases, the severity of aerothermal heating increases exponentially [1,2]. A leading edge curvature of the order of a millimeter experiences stagnation heat fluxes of the order of 10 MW/m^2, making it essential to develop a highly effective thermal protection system (TPS) for sharp leading edges. Traditional TPS technologies, such as radiative surfaces or ablative heat shields, are inadequate for these demands. Refractory materials often used as radiative surfaces, such as carbon-fiber-reinforced carbon composites [3,4], are susceptible to oxidation and weight loss, especially when dealing with sharp leading edges where the stagnation heat fluxes can easily surpass the limits of thermal radiation cooling. Ablative heat shields [5], such as those made using phenolic impregnated carbon ablator (PICA) [6,7], can endure higher rates of heating, but they undergo significant shape change as the material ablates. Hence, TPS capable of mitigating substantial heating without inducing shape alteration during flights, such as transpiration cooling employing gases, liquids [8,9], or electrons [10–12], is imperative.

Transpiration cooling using gas or a liquid coolant is a promising technology for providing effective thermal protection to sharp leading edges [8,9]. This TPS involves a porous leading edge through which a working fluid flows to absorb and dissipate heat at the

surface. For gaseous transpiration cooling, coolant gas is injected by an applied force through the porous leading edge. Cold gas from the reservoir exchanges energy with the hot leading edge to absorb the heat before discharging into the external flow. While previous studies have demonstrated the effectiveness of gaseous transpiration cooling in simulated hypersonic environments [13–21], such systems require a large mass flow rate and a large reservoir volume, which could lead to decreased lift-to-drag ratios.

To overcome the limitations of gas transpiration cooling, recent studies [22–28] explored transpiration cooling utilizing liquid coolants that take advantage of the latent heat of phase change. Figure 1 depicts the schematic of transpiration-cooling TPS using liquid coolants. In this TPS, the liquid coolant flows from a reservoir inside the flight vehicle through a porous leading edge by the external pressure and/or the internal capillary force. Once the liquid coolant reaches the surface, it absorbs the incident heat flux from the external hypersonic flow through a liquid-to-vapor phase change and discharges into the hypersonic flow as vapor.

The potential of transpiration cooling using liquid coolant has been demonstrated by various experimental studies. For example, Van Foreest et al. [22] experimentally showed the effectiveness of transpiration cooling by subjecting a leading edge composed of porous alumina ceramic to a simulated hypersonic flow using an arcjet test facility. They used liquid water as the working fluid and reduced the maximum stagnation temperature of the leading edge from 1900 to 500 K. However, the TPS required an external system to deliver the coolant through the leading edge, which can be expensive and cumbersome for practical hypersonic vehicles. To eliminate the use of an external pumping system, Huang et al. [27] incorporated transpiration cooling that solely relied on capillary action to deliver the flow. They subjected a circular copper coupon equipped with transpiration cooling using liquid water as the coolant and a hydrophilic porous medium to facilitate the capillary action. They successfully maintained the maximum temperature of the coupon below 373K. However, their system was limited to a maximum heat flux of 1 MW/m^2 due to the self-pumping capability of the porous media.

To address the above challenges of transpiration cooling using water, we demonstrate a new concept of transpiration cooling using oxides as the working fluid in our study. In this TPS, solid oxide may be delivered toward the leading edge using a mechanical system such as a spring–piston assembly. The solid melts, and then the molten liquid flows through the porous medium to reach the surface. The liquid evaporates at the surface to absorb the incident heat flux and discharges into the external hypersonic flow. Figure 2 depicts a schematic of transpiration cooling utilizing oxide coolant. Oxide coolants provide several advantages over water. High surface energies of molten oxides can increase the internal capillary force and thereby enhance the capillary-driven flow through the porous leading edge. This reduces or potentially eliminates the need for an external liquid pumping system. Furthermore, oxides provide great chemical resistance against the highly energetic atomic oxygen present in the hypersonic flow. Their wide range of available material properties also facilitates material selection that maximizes the performance of transpiration cooling for a given flight trajectory or application. Previous studies on gas transpiration cooling [13] have shown that certain material properties, such as heat capacity and molar mass, can significantly influence the capability of TPS. For transpiration cooling using liquid coolant, other material properties, including the latent heat of phase change and the saturation temperature, are also critical.

Many previous works [25,29–34] have numerically characterized the evaporation process in hypersonic flows. However, these studies assumed the evaporating surface to be in a state of thermodynamic equilibrium. This assumption is only valid when the maximum mass transfer rate at the surface is limited by the diffusion rate through the boundary layer. At the stagnation point of sharp leading edges, the maximum mass diffusion rate through the boundary layer can be

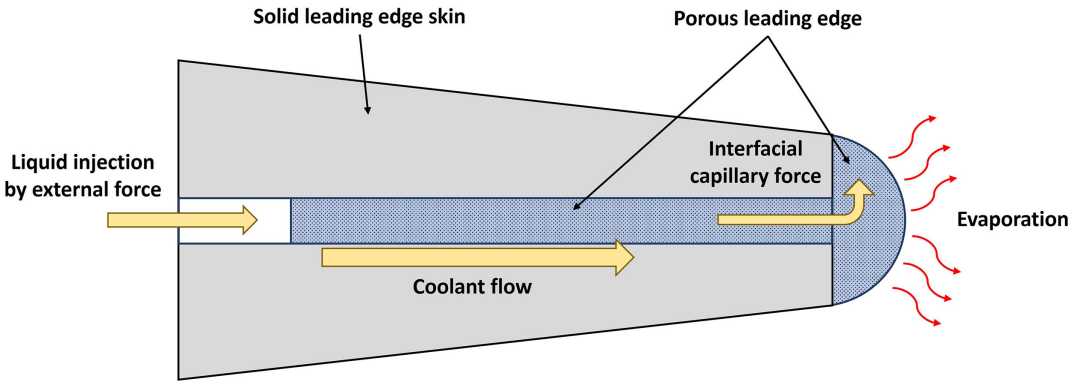

Fig. 1 Schematic of transpiration-cooling TPS utilizing liquid coolant and porous leading edge.

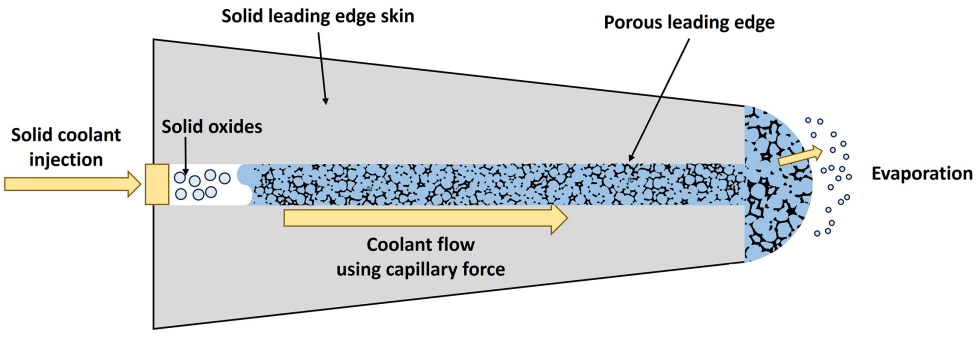

Fig. 2 Schematic of transpiration-cooling TPS utilizing oxide coolant.

significant, potentially exceeding the maximum mass transfer rate predicted by the kinetic theory [35,36]. The thermodynamic equilibrium assumption can thereby lead to considerable underprediction of the surface temperature [37,38]. An unexpectedly high surface temperature is of great concern since it can lead to the two main modes of failure of the TPS: softening or melting of the porous leading edge and nucleation of vapor bubbles within the porous flow paths, which disrupt the coolant flow to the surface and cause surface dry-out [25,39]. Recent studies of the turbulence transition and recession of molten oxide layers during ablation have considered thermodynamic nonequilibrium conditions at the surface to characterize heat and mass transfer along the leading edge surface [40–43]. But to our knowledge, there has been no systematic study of evaporative transpiration cooling accounting for thermodynamic nonequilibrium conditions.

In this study, we numerically illustrate the potential of transpiration cooling using oxide coolants as a new alternative system to thermally protect sharp leading edges. We study evaporative transpiration cooling under thermodynamic nonequilibrium conditions and examine the effects of coolant material properties, flight conditions, and leading edge radii on the surface temperature, evaporative mass flux, and boiling limit. To this end, we utilize both the 2D axisymmetric boundary-layer theory and direct numerical simulation (DNS) utilizing a third-order shock-fitting finite difference scheme considering steady-state solutions with thermochemical nonequilibrium to model the evaporation process over a sharp, hemispherical leading edge. In the following, we first present a semi-analytic model using the boundary-layer theory derived at the stagnation point to parametrically characterize the TPS performance over a wide range of flight conditions, leading edge radii, and material properties. We then discuss the results from DNS for nine representative flight conditions and a set of seven representative materials to validate the boundary-layer model. Using DNS, we further analyze the effect of chemical reactions between the oxide vapor and the external hypersonic flow.

II. Hypersonic Flow Models

A. Semi-Analytic Boundary-Layer Model

We develop a semi-analytic model derived from the 2D axisymmetric boundary-layer theory to parametrically investigate the evaporation process at the stagnation point of a sharp, hemispherical leading edge. A schematic of the model is shown in Fig. 3. We assume a frozen boundary layer with a ternary mixture of molecular air, dissociated air, and oxide vapor. The governing steady-state equations are [44]

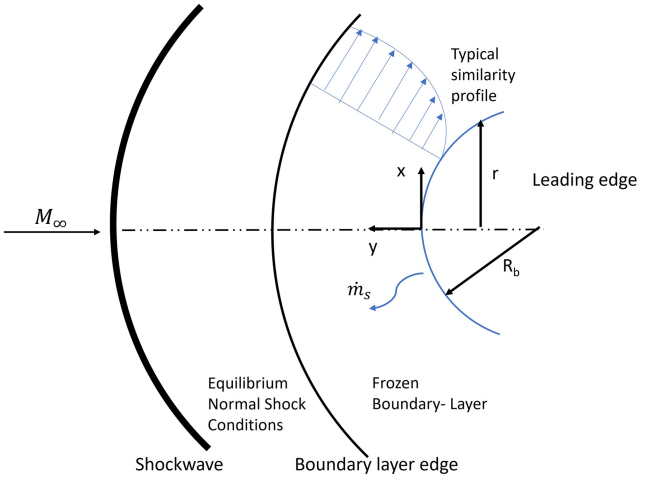

Fig. 3 Schematic and the coordinate system at the stagnation point of a hypersonic leading edge.

$$\frac{\partial}{\partial x}(\rho u_x r) + \frac{\partial}{\partial y}(\rho u_y r) = 0 \tag{1}$$

$$\rho u_x \frac{\partial u_x}{\partial x} + \rho u_y \frac{\partial u_x}{\partial y} = -\frac{\partial P}{\partial x} + \frac{\partial}{\partial y}\left(\mu \frac{\partial u}{\partial y}\right) \tag{2}$$

$$\rho\left(u_x \frac{\partial h}{\partial x} + u_y \frac{\partial h}{\partial y}\right) = u_x \frac{\partial P}{\partial x} + \mu\left(\frac{\partial u}{\partial y}\right)^2 + \frac{\partial}{\partial y}\left(k \frac{\partial T}{\partial y}\right) - \sum_i j_i \frac{\partial h_i}{\partial y} \tag{3}$$

$$\rho u_x \frac{\partial C_i}{\partial x} + \rho u_y \frac{\partial C_i}{\partial y} + \frac{\partial}{\partial y}(\rho_i j_i) = 0 \tag{4}$$

Equations (1–4) represent the conservation of mass, momentum, energy, and species, respectively. We assume that the mass transfer within the boundary layer is dominated by Fick's diffusion, where the diffusive mass flux j in Eqs. (3) and (4) is given as [45]

$$j_i = \sum_{j \neq i} \frac{M_i M_j}{M^2} \rho D_{ij} \frac{\partial X_j}{\partial y} \tag{5}$$

for a system consisting of more than two species. The diffusive flux is then related to the surface mass transfer rate by the following equation:

$$\dot{m}_{c,s} = \frac{j_{c,s}}{1 - C_{c,s}} \tag{6}$$

We use the Lees–Dorodnitsyn transformation [44] to transform the governing partial differential equations to ordinary differential equations as a function of the similarity variable η. The transformation defines η as

$$\eta = \frac{u_e}{\sqrt{2\varepsilon}} \int_0^y \rho r \, \mathrm{d}y \tag{7}$$

where ε is defined as

$$\varepsilon = \int_0^x \rho_s \mu_s u_e r^2 \, \mathrm{d}x \tag{8}$$

Thus, the governing equations are

$$(lf'')' + ff'' + \frac{1}{2}\left(\frac{\rho_e}{\rho} - f'^2\right) = 0 \tag{9}$$

$$\left(\frac{l}{Pr} c_p \theta'\right)' + f c_p \theta' - \frac{l}{Pr} \frac{\theta'}{M^2} \sum_i c_{p,i} M_i \left(\sum_{j \neq i} M_i Le_{ij} X_j'\right) = 0 \tag{10}$$

$$\frac{M_i}{M} f\left(\frac{M'}{M} X_i - X_i'\right) + \left(\frac{l}{Pr} \frac{1}{M^2} \sum_{j \neq i} M_i M_j Le_{ij} X_j'\right)' = 0 \tag{11}$$

where each prime symbol denotes differentiation with respect to the similarity variable. f is the similarity stream function defined such that $f' = u/u_e$ and θ is the nondimensional temperature defined as T/T_e. We consider the boundary-layer edge conditions to equal those behind a normal shock under chemical equilibrium. For a given flight condition, the edge conditions are obtained from Wittliff and Curtis [46]. We assume that the leading edge surface is impermeable and fully catalytic to the air species. Note that, because the surface is fully catalytic, the surface heat and mass

transfer behavior at the surface are virtually identical under both frozen and local equilibrium assumptions [2]. The boundary conditions for Eqs. (9–11) are

$$\begin{aligned} \eta = 0: \quad & f = f_s \qquad \eta \to \infty: \quad f' = 1 \\ & f' = 0 \qquad\qquad\quad \theta = 1 \\ & \theta = \theta_s \qquad\qquad\quad C_a = C_{a,e} \\ & C_a = 0 \qquad\qquad\quad C_k = 0 \\ & C_k = C_{k,s} \end{aligned}$$

We use the shooting method [47] to convert the boundary value problem to an initial value problem at the surface. The values of f'', θ', C_a', and C_k' are numerically iterated to obtain the solution that satisfies the above boundary conditions.

B. Thermochemical Nonequilibrium DNS

To more rigorously model the complex thermochemical behavior of the hypersonic flow in the presence of evaporative transpiration, we utilize a steady-state flow solver with a third-order finite difference scheme and a shock-fitting algorithm to solve the governing equations. Details of the model and validation of its solutions against experimental data can be found in [40,41,48,49]. The governing equations are formulated for thermochemical nonequilibrium flows using $5 + n$ nonionizing species (N_2, O_2, NO, N, O, and oxide vapor) and a two-temperature model. The two-temperature model represents the translational and rotational energy, which are assumed to be in equilibrium, and the vibrational energy. Rotational energy modes are assumed to be fully excited. The resulting governing equations are the $5 + n$ mass conservation equations, three momentum-conservation equations, total energy conservation equation, and vibrational energy conservation equation. In the vector form, the governing equation is

$$\frac{\partial U}{\partial t} + \frac{\partial F_j}{\partial x_j} + \frac{\partial G_j}{\partial x_j} = W \tag{12}$$

where U represents the state vector of conserved quantities, F_j represents the inviscid flux vector, G_j represents the viscous flux vector in jth direction, and W represents the source terms. U and W are defined as

$$U = \begin{bmatrix} \rho_i \\ \dots \\ \rho_N \\ \rho u_x \\ \rho u_y \\ \rho u_z \\ \rho e \\ \rho e_v \end{bmatrix} \qquad W = \begin{bmatrix} \omega_i \\ \dots \\ \omega_N \\ 0 \\ 0 \\ 0 \\ 0 \\ \sum_{j=1}^{\mathrm{NMS}} (Q_{T-V,j} + \omega_j e_{v,j}) \end{bmatrix} \tag{13}$$

where subscript N is the number of species, and superscript "NMS" is the number of molecular species. F_j and G_j are defined as

$$F_j = \begin{bmatrix} \rho_1 u_j \\ \dots \\ \rho_N u_j \\ \rho u_x u_j + p\delta_{1j} \\ \rho u_y u_j + p\delta_{2j} \\ \rho u_z u_j + p\delta_{3j} \\ (p + \rho e) u_j \\ \rho e_v u_j \end{bmatrix}$$

$$G_j = \begin{bmatrix} \rho_1 v_{1j} \\ \dots \\ \rho_N v_{N,j} \\ \tau_{1j} \\ \tau_{2j} \\ \tau_{3j} \\ -u_i \tau_{ij} - k_T \dfrac{\partial T}{\partial x_j} - k_v \dfrac{\partial T_v}{\partial x_j} + \sum_{k=1}^{\mathrm{NMS}} \rho_k h_k v_{k,j} \\ -k_v \dfrac{\partial T_v}{\partial x_j} + \sum_{k=1}^{\mathrm{NMS}} \rho_k h_k v_{k,j} \end{bmatrix} \tag{14}$$

Here, $\nu_{k,j}$ is the species diffusion velocity, defined as $\nu_{k,j} = (-D_k/C_k)\partial C_k/\partial x_j$, and $\tau_{i,j}$ is the viscous stress tensor, defined as $\tau_{i,j} = \mu(\partial u_i/\partial x_j + \partial u_j/\partial x_i) - \delta_{ij}(2\mu/3)\partial u_k/\partial x_k$. We define the total energy per unit volume as

$$\rho e = \sum_{i=1}^{N} \rho_i c_{v,i} T + \rho e_v + \frac{1}{2}\rho(u_x^2 + u_y^2 + u_z^2) + \rho_i h_{f,i}^{\circ} \tag{15}$$

where $h_{f,i}^{\circ}$ is the heat of formation at the standard conditions and $c_{v,i}$ is the translation-rotation specific heat at constant volume. We also define the total vibrational energy per unit volume as

$$\rho e_v = \sum_{i=1}^{\mathrm{NMS}} \rho_i \left(\sum_{j=1}^{\mathrm{NMD}} \frac{g_{i,j} R}{M_i} \frac{\theta_{v,i,j}}{\exp(\theta_{v,i,j}/T_v) - 1} \right) \tag{16}$$

Here, "NMD" denotes the number of vibrational modes for molecule i, $\theta_{v,i,j}$ is the characteristic temperature of each vibrational mode, and $g_{i,j}$ is the degeneracy of each vibrational mode. Characteristic vibrational temperatures and the degeneracy of molecular air species (N_2, O_2, and NO) are taken from Park [50].

We characterize the energy exchange between the translational–rotational and vibrational temperatures using the Landau–Teller formulation given as

$$Q_{T-V,i} = \rho_i \frac{e_{v,i}(T) - e_{v,i}(T_v)}{\langle \tau_i \rangle + \tau_{cs}} \tag{17}$$

where $\langle \tau_i \rangle$ is the Landau–Teller vibrational relaxation time given by Lee [51] and τ_{cs} is from Park [50].

C. Evaporation and Chemistry Model

To characterize the evaporation process under thermodynamic nonequilibrium conditions, we use the Hertz–Knudsen equation

[38,41,42] derived from the kinetic theory. For an evaporating species c, the mass transfer rate due to evaporation at the surface is

$$\dot{m}_s = \alpha \sqrt{\frac{M}{2\pi R T_s}} (P_{eq} - P_s) \tag{18}$$

where P_{eq} is the saturation pressure at a given surface temperature for species c as calculated by the integrated form of the Clausius–Clapeyron equation:

$$P_{\text{eq}} = P^* \exp\left[\frac{L}{R}\left(\frac{1}{T^*} - \frac{1}{T_s}\right)\right] \tag{19}$$

The superscript "*" indicates the saturation condition at 1 atm pressure. The accommodation coefficient α depends on the molecular collisions at the liquid–gas interface. We assume α to be equal to one, which is typical for most liquids [35]. By incorporating the Hertz–Knudsen equation, the evaporative mass flux at the surface depends on both the surface temperature and the mole fraction. The mass transfer rate is then coupled to the mass diffusion behavior through the boundary layer of the external hypersonic flow by Eq. (6).

The energy exchange due to the phase change is also coupled between the surface and the flow by the conservation of energy at the surface

$$k_T \frac{\partial T}{\partial y} + k_v \frac{\partial T_v}{\partial y} + \sum_i \rho h_i D \frac{\partial C_i}{\partial y} = \sigma \epsilon T^4 + \dot{m} \sum_i C_i h_{i,o} \tag{20}$$

where σ is the Stefan–Boltzmann constant, and $h_{i,o}$ is defined as

$$h_{i,o} = c_{p,i} T + e_{v,i} + h^\circ_{f,i} + \frac{1}{2}\left(u_x^2 + u_y^2 + u_z^2\right) \tag{21}$$

We assume that the radiative heat flux from the external hypersonic flow to the surface is negligible. We also assume that the conductive heat flux into the leading edge increases the temperature of the liquid coolant from room temperature to the surface temperature.

We estimate the viscosity and thermal conductivity of air and evaporated species using Blottner's relationship [49,52]. For air species, we obtained the coefficients from Blottner et al. [52] and Gupta et al. [53]. For evaporating species, we use rigid-sphere kinetic theory to estimate the transport properties [45]. We estimate the kinetic diameter of evaporated species as a linear function of their molar mass using the data presented in [54]. We then calculate the mixture's viscosity and thermal conductivity using Wilke's semi-empirical relationships [55]. We also assume that the diffusivity of each species is equal to the mixture diffusivity as determined by the mixture viscosity and a constant Schmidt number of 0.5 [49].

We consider a range of latent heats of evaporation from 100 to 800 kJ/mol, molar masses from 10 to 200 g/mol, and T^* from 1500 to 3500 K. We chose these ranges to encompass those of typical oxides obtained from [56], as shown by the shaded regions in Fig. 4. Values within the dashed rectangles are used to perform the parametric study using the boundary-layer model. Our DNS model uses a set of seven different representative materials, marked with symbols in Fig. 4, with properties emulating those of typical oxides. The properties of these seven materials are also tabulated in Table 1.

Our DNS model implements a chemical nonequilibrium model for air species consisting of three dissociation reactions and three exchange reactions. We obtain the forward reaction rates and equilibrium constants of each reaction from Park [57], Bhutta and Lewis [58], and Park et al. [59]. The backward reaction rates and constants are calculated from the forward rates and equilibrium constants using the following relationship:

$$K_{\text{back}} = \frac{K_{\text{forward}}}{K_{\text{eq}}} \tag{22}$$

The equilibrium constants are computed either using the curve fits from Park and McBride [50,60] or using the Gibbs free energy of formation of the corresponding reaction obtained from NIST-JANAF thermodynamic table [61].

To study the effects of the chemical reaction between the oxide vapor and the external hypersonic flow, we consider two specific materials, namely, barium oxide (BaO) and silicon dioxide (SiO_2). The two materials are potential candidates for coolants [32,42,62,63]. For BaO, we consider the following endothermic reaction:

$$\text{BaO} \rightarrow \text{Ba} + \text{O} \tag{23}$$

where the evaporated BaO vapor dissociates into its elemental form. For SiO_2, we assume the following endothermic reaction:

$$\text{SiO}_2 \rightarrow \text{SiO} + \text{O} \tag{24}$$

where the evaporated SiO_2 vapor dissociates into SiO and atomic oxygen. We neglect the dissociation of SiO into its elemental form since the results in Sec. IV showed negligible dissociation of SiO_2.

Table 1 Set of seven materials used in DNS to emulate the properties of typical oxides

Material	L, kJ/mol	M, g/mol	T^*, K
A	300	30	2773
B	600	90	3273
C	300	150	2273
D	150	90	2273
E	300	90	3273
F	300	150	2773
G	600	90	2273

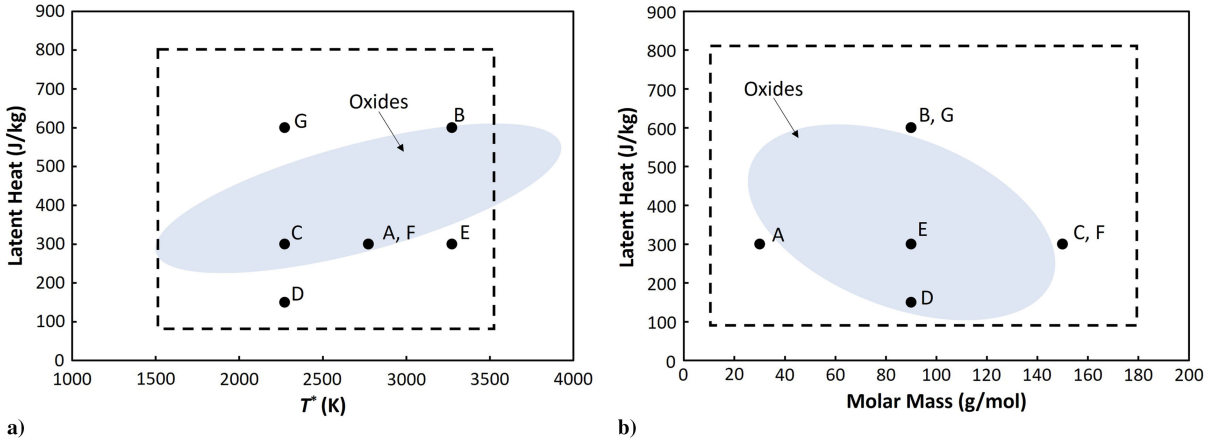

Fig. 4 Ranges of the material properties considered in our models: a) latent heat vs T^*; b) latent heat vs molar mass.

We obtain the heats of reaction and the equilibrium constants from the NIST-JANAF thermochemical table [61]. We obtain the forward reaction rates for the two reactions from Johnston [64]. The reaction rate of BaO dissociation has not been reported, and we estimate that it is similar to that of MgO dissociation provided in [64]. The backward reaction rates are again calculated using the forward reaction rate and the equilibrium constants using Eq. (22). We also perform a parametric study varying these rates by a factor of 10^6 to highlight the effects of the chemical reaction with the external hypersonic flow.

D. Validation of the Models

The DNS algorithms, chemical equations, boundary conditions, and vaporization process, as detailed above, have been validated against experimental data for a 5-species air model and an 11-species model with carbon ablation. The validation of DNS algorithms and the 5-species nonequilibrium model is detailed in [48], while the 11-species model, including the boundary conditions that describe the ablation of carbon, is detailed in [49]. This validation study consisted of comparisons between the DNS results of [49] and three previous numerical studies from established literature. Comparisons showed excellent agreement of temperature and species concentration, with explainable disagreement near the shock. The disagreement was concluded to arise due to differences between the shock-fitting algorithms used in [49] and the shock-capturing algorithms used in the previous studies.

The 6-species code for materials A–G and the 7-species code used for BaO and SiO_2 are algorithmically the same as the 11-species code. Hence, the validation studies of the code in [49] serve to validate the DNS code used in this study.

The only distinction between the 11-species DNS code and the DNS code used in this study is in the reaction rate data used to determine the rate of production of chemical species. As such, the chemical equilibrium constant and reaction rates were confirmed to vary with temperature as described in the literature [50,60,61,64], validating the changes made to the DNS code.

As an additional precaution, a grid refinement study was run on the DNS code. Solutions for material D at Mach 20 and 30 km altitude with grid sizes of 30×80, 60×160, and 120×320 were compared to a solution with a 240×640 grid. It was found that there was at most a 0.33% difference in the stagnation point pressure among the different grid sizes. Due to the complicated nature of the DNS algorithms and especially due to the complicated boundary conditions being used, the 1/8th error ratio is not typically observed from doubling grid sizes. Instead, a solution is considered grid-independent if the solutions are less than 1% different at the stagnation point after doubling the grid. Therefore, the close agreement between all converged solutions shows that the solution is grid-independent. The 120×320 grid size was used throughout the rest of this study for increased resolution near the stagnation point and added safety in the accuracy of solutions at different flight conditions with different materials. Solutions were obtained using TACC's Stampede 2 and Purdue's ANVIL high-performance computing clusters. Stampede 2's SKX compute nodes consisted of two sets of 24 cores per every socket, while ANVIL's standard compute nodes have 128 cores per every socket. Baseline solutions with no coolant were obtained, and then the wall boundary conditions were changed to incorporate coolant evaporation for each material. By using the converged solutions with no coolant mass flux as a starting point, we were able to obtain converged results for most of the DNS cases studied in a few hundred thousand time steps.

Because materials A through G are theoretical, the results here cannot be compared directly to those of an experimental study. Instead, the results from the semi-analytical boundary-layer model are validated by comparing them with the results from the validated DNS code. The results between these two methods vary at worst less than 5% in the surface temperature at the stagnation point for all trials, with a majority of cases seeing less than 2% difference. This discrepancy is small considering the extensive assumptions made in the boundary-layer model, namely, the frozen flow and fully catalytic wall conditions. The maximum difference in surface mass flux of coolant is 25% between each method of solution, with most results having a discrepancy of less than 8%. The incident heat flux at the stagnation point is 16.4% larger from the DNS results than the incident heat flux from the boundary-layer model. A possible reason for the discrepancy is due to the distinction between the fully catalytic boundary condition of the boundary-layer theory and the chemical nonequilibrium boundary condition of the DNS code. The fully catalytic boundary condition forces recombination of atomic species at the stagnation point, resulting in a surface heat flux in the boundary-layer solutions that is not present in the DNS solutions. Instead, the incident heat flux from the DNS solutions is due entirely to conduction at the stagnation point.

The leading edge surface heat flux is expected to be larger for fully catalytic walls, as discussed in [2]; however, it is the opposite in this case. We hypothesize that the large mass fraction of evaporating species at the surface reduces the diffusion rate of atomic air species to the surface, decreasing the magnitude of heat flux due to the recombination of such species. The frozen flow assumption of the boundary-layer model also amplifies this effect because the contribution of recombination heat flux is the largest under this assumption. Conversely, the surface heat flux in the DNS results is solely due to the gradient in the temperature profile, which may not be altered significantly by the large mass fraction of evaporating species at the wall.

The components of the wall heat flux at the stagnation point for each model can be seen in Table 2, considering material D at Mach 20 and 20 km, which had the largest disagreement between DNS and the boundary-layer model.

Figure 5 shows a comparison between the stagnation line solution provided by DNS and the boundary-layer model for temperature as a function of distance downstream of the shock. The stagnation point is located at the right-most bound of the x axis. Solutions end at the theoretical boundary-layer edge on the left-most boundary of the plot. The results shown are for material D at Mach 20 and 20 km, which had the largest disagreement between DNS and the boundary-layer model. The comparatively larger conduction heat flux of the DNS solutions can be seen by the correspondingly larger slope near the wall surface. This increased heat flux, as well as the increased stagnation point temperature, serve to keep the temperature profile from the DNS results above the temperature profile of the boundary-layer model along the entire stagnation line. The ratio of stagnation point mass fraction from DNS and the boundary-layer model seen in Fig. 5 is equivalent to the ratio of incident heat fluxes in Table 2, meaning that the larger stagnation point mass fraction predicted by DNS is proportionally related to the larger incident heat flux predicted by DNS. This serves to show that the discrepancy between the two models is driven by the difference in the incident heat fluxes at the stagnation point due to the high mass fraction of evaporating species and the fully catalytic boundary condition assumed by the boundary-layer model. Overall agreement between the stagnation line profiles

Table 2 Stagnation point heat fluxes between DNS and the boundary-layer model[a]

Incident heat flux	DNS, MW/m^2	Boundary-layer model, MW/m^2	Cooling heat flux	DNS, MW/m^2	Boundary-layer model, MW/m^2
Conduction	52.2	21.0	Evaporation	48.5	37.8
Recombination	0	19.5	Radiation	3.6	2.7
Total incident heat flux	52.2	40.5	Total cooling heat flux	52.1	40.5

[a]Discrepancy is driven due to the difference in the recombination heat fluxes

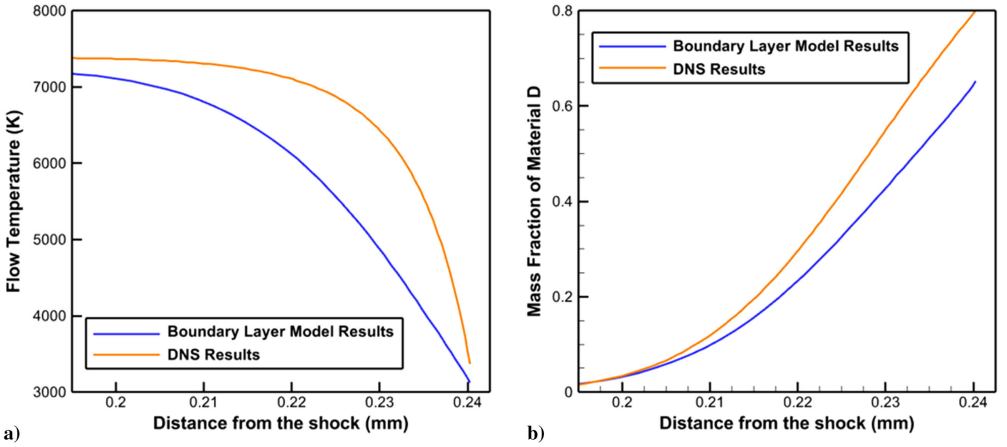

Fig. 5 Stagnation line solutions for a) flow temperature and b) mass fraction of material D as a function of distance downstream of the shock.

is good, however, with similar values in flow temperature between the two models at the stagnation point and edge of the boundary layer. The shape of the boundary-layer temperature profiles is similar as well, with the DNS possessing a sharper gradient near the stagnation point for the reasons discussed so far.

Due to the validation of current DNS algorithms and the close agreement between the two current methods of solution, the boundary-layer theory used here is shown to be validated.

III. Parametric Analysis in Frozen Flow

We now present the effect of material properties, flight conditions, and leading edge radii on the performance of transpiration cooling. We quantify the performance of the TPS using three metrics: surface temperature, evaporative mass flux, and boiling limit factor of safety. The operating surface temperature of a TPS sets the limit on the materials that can be used to construct the leading edge skin or the porous medium. A small evaporative mass flux may be desired to reduce the risk of drying out at the surface and lower the cost and weight of TPS. The temperature within the porous leading edge must not exceed the saturation temperature of the coolant at the stagnation pressure to avoid nucleation that could block the flow and disrupt continuous coolant delivery to the surface. To assess this, we define the boiling limit factor of safety, F_s, as the ratio between the saturation temperature, T_{eq}, and the surface temperature at the stagnation point, T_s:

$$F_s = \frac{T_{\text{eq}}}{T_s} \tag{25}$$

T_{eq} is calculated using the Clausius–Clapeyron equation [Eq. (19)] rearranged as follows:

$$T_{\text{eq}} = \left[-\frac{R}{L} \ell_n \left(\frac{P_s}{P^*} \right) + \frac{1}{T^*} \right]^{-1} \tag{26}$$

When the value of F_s is equal to or less than one, vapor nucleation within the porous leading edge can occur and disrupt the coolant flow to the surface.

A. Material Property

We first discuss the effect of the coolant material properties: the latent heat of evaporation, molar mass, and T^* of the coolant. These three material properties govern the heat and mass transfer behavior at the surface [Eqs. (18) and (19)]. We vary the latent heat of evaporation from 100 to 800 kJ/mol, the molar mass from 10 to 200 g/mol, and T^* from 1500 to 3500 K to encompass the properties of typical oxides. Here, we fix the altitude, the speed, and the leading edge radius as constants at 30 km, Mach 15, and 3.1 mm, respectively, to isolate the effect of variation in the material properties. Figures 6–11 illustrate the surface temperature, evaporative mass

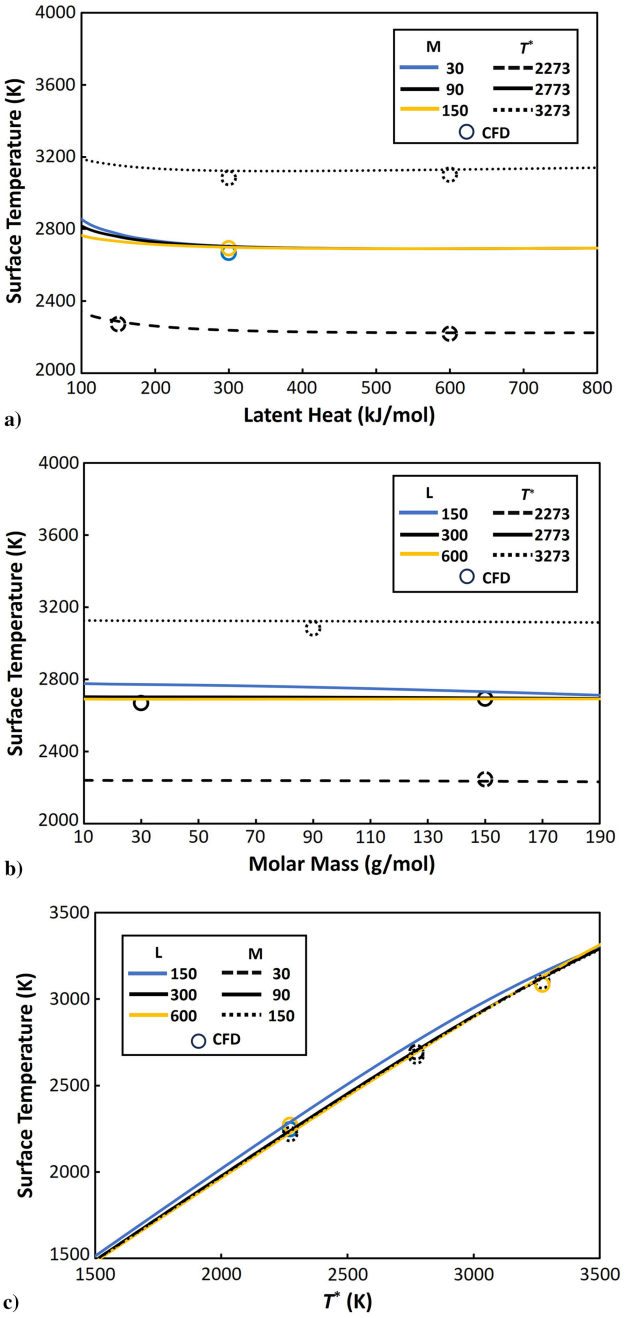

Fig. 6 Predicted surface temperature as a function of the a) latent heat of evaporation, b) molar mass, and c) T^*.

flux, and F_s as a function of the three material properties. The DNS results are also shown as symbols for comparison.

Figure 6 shows the relationship between the surface temperature of the leading edge and the three material properties. Line colors and dash types represent the variation in material properties not shown in the x axis. Symbols are obtained from DNS and have a less than 2% difference with the boundary-layer model results. Figure 7 shows the predicted color contour of the mole fraction for materials B and E. The left-most boundary of the contour is immediately behind the shock, and the right-most boundary of the contour is the leading edge surface. X is the distance from the shock, and Y is the distance from the stagnation line.

We find that the surface temperature shows negligible change as a function of the latent heat and the molar mass. One might expect from Eqs. (18) and (19) that a higher latent heat would lower the surface temperature since one can achieve a higher evaporative heat flux for a given evaporative mass flux. However, as seen in Fig. 7 material B has a lower mole fraction of evaporating species at the surface than material E. Material B also has a higher latent heat than material E. This shows that higher latent heat leads to a lower mole fraction of evaporating species at the surface. A lower mole fraction at the surface reduces the vapor shielding effect, which thereby leads to an increase in the incident heat flux, as shown in Fig. 8. This increase in the incident heat flux requires a higher evaporative heat flux and, thereby, a higher surface temperature. These two opposing effects counteract each other, and the change in latent heat appears to have a negligible impact on the surface temperature. Similarly, one might expect that a lower molar mass would lower the surface temperature since the evaporative heat flux is proportional to $M^{-1/2}$. However, as shown in Fig. 9, the incident heat flux increases as molar mass decreases because heavier species enhance the thermal shielding effect. The diffusivity of gas molecules is proportional to $M^{-1/2}$. This increase in the incident heat flux leads to a higher evaporative mass flux and, thus, higher surface temperature. Again, these two opposing behaviors make the surface temperature nearly independent of the molar mass. The predicted surface temperature, in contrast, is proportional to T^* of the coolant material. Because the mass transfer rate is proportional to $\exp^{(1/T^*-1/T_s)}$, the surface temperature must be very close to T^* to have meaningful mass transfer rates.

These relationships suggest that only the T^* of the coolant material controls the operating surface temperature of the TPS. Hence, the thermal limit of the porous leading edge must be larger than T^* at a given flight condition to avoid failure.

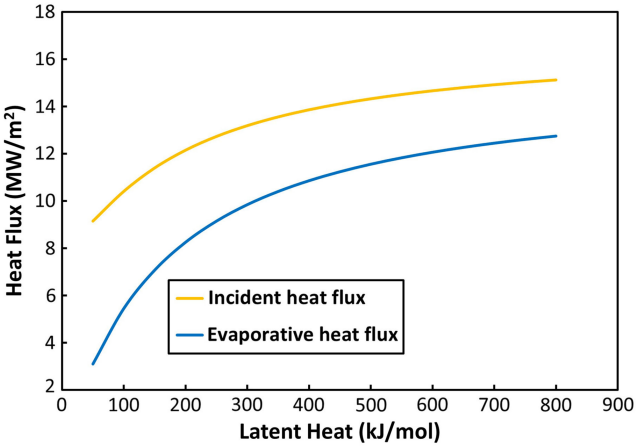

Fig. 8 Predicted surface heat fluxes as a function of the latent heat. The molar mass and T^* of the material are 90 g/mol and 2773 K.

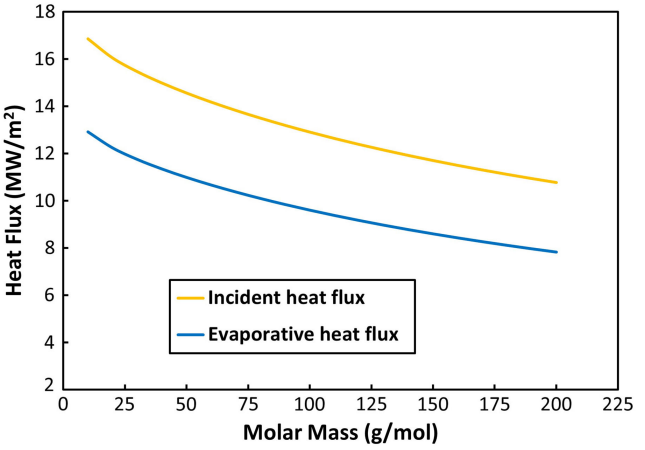

Fig. 9 Predicted surface heat fluxes as a function of molar mass. Latent heat and T^* of the material are 300 kJ/mol and 2773 K.

Figure 10 shows the relationship between the evaporative mass flux and the three material properties. Line colors and dash types represent the variation in material properties not shown on the axis. Symbols are obtained from DNS and have a less than 8% difference

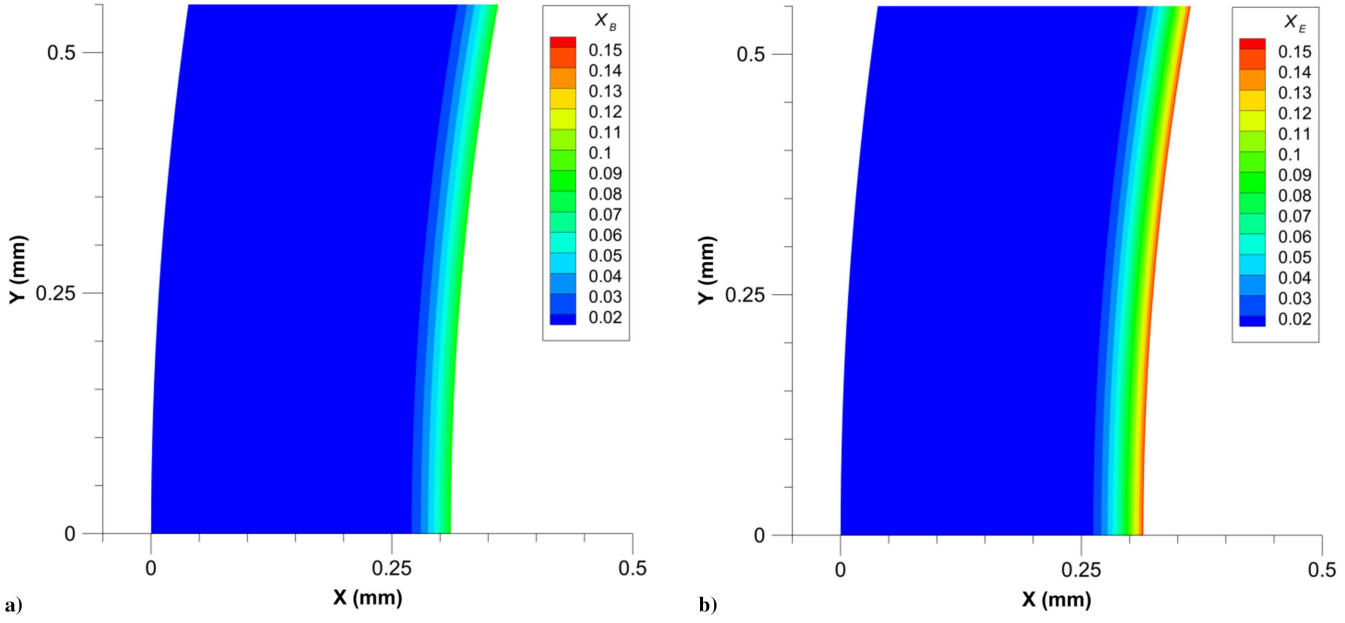

Fig. 7 Predicted color contour of mole fraction for a) material B and b) material E.

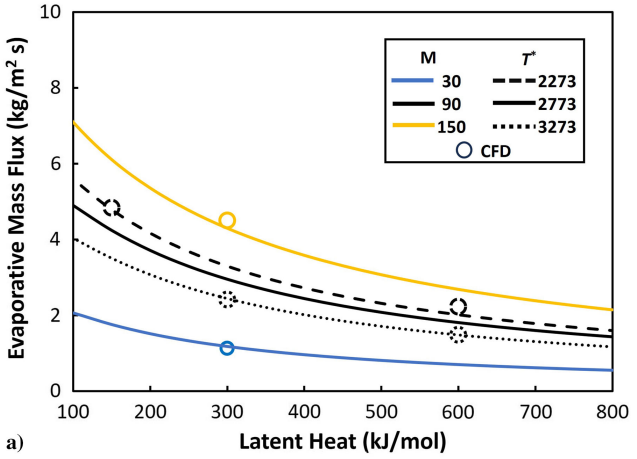

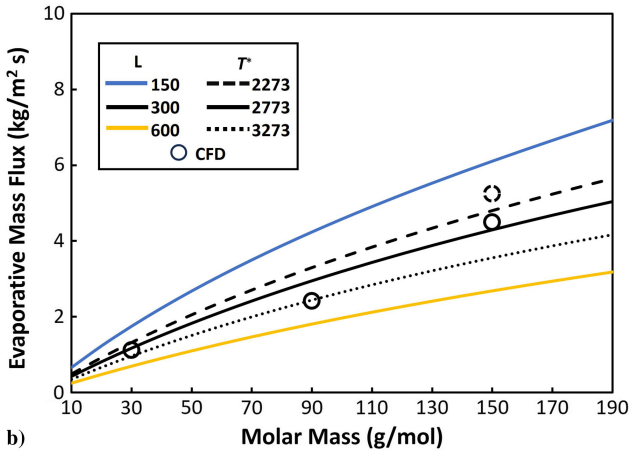

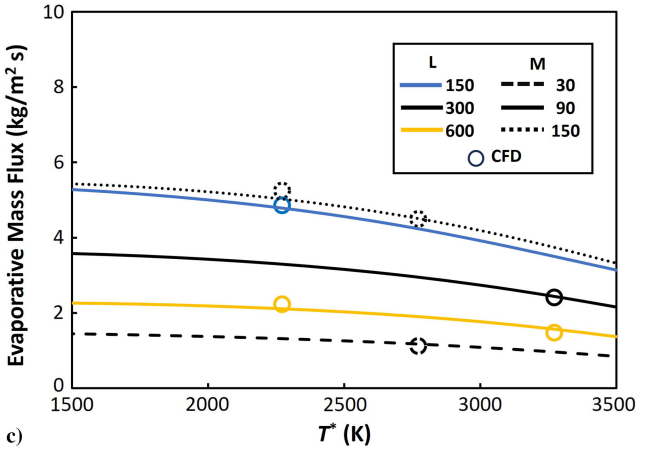

Fig. 10 Predicted evaporative mass flux as a function of the a) latent heat of evaporation, b) molar mass, and c) T^*.

with the boundary-layer model results. We find that evaporative mass flux is influenced by all three properties. A higher latent heat or a lower molar mass increases the specific latent heat of the material, reducing the mass transfer rate needed to absorb a given amount of incident energy. Although a higher latent heat and a lower molar mass increase the incident heat flux by approximately 50%, as shown in Figs. 8 and 9, the change in the specific latent heat is greater (a factor of 8–10), resulting in lower evaporative mass fluxes. The evaporative mass flux also slightly decreases as T^* increases. Since the surface temperature is proportional to T^*, higher T^* leads to a lower incident heat flux by reducing the temperature gradient and promoting thermal radiation cooling at the surface. Hence, the coolant material with a higher specific heat and a higher T^* is desired to minimize the required evaporative heat flux of the TPS. However, increasing the latent heat beyond approximately 500 kJ/mol gives a diminishing return in reducing the evaporative mass flux due to an increase in the incident heat flux at the surface, as shown in Fig. 8.

Figure 11 shows the relationship between F_s and the three material properties. Line colors and dash types represent the variation in material properties not shown on the axis. Symbols are obtained from DNS and have a less than 2% difference with the boundary-layer model results. We find that F_s is nearly independent of the molar mass since the molar mass does not significantly affect the surface temperature or the saturation condition, as illustrated in Fig. 6 and Eq. (26). The surface temperature is also nearly independent of the latent heat; however, a higher latent heat decreases T_{eq} as given by Eq. (26) leading to a decrease in F_s. We also find that higher T^* leads to an increase in F_s. The surface temperature, which is the denominator of F_s, is approximately proportional to T^*, as shown in

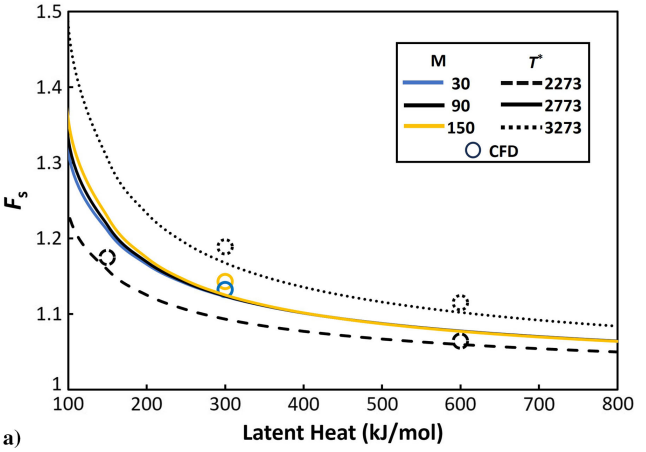

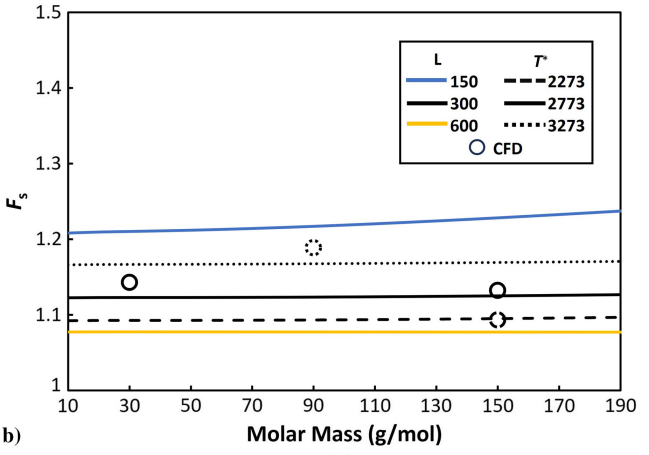

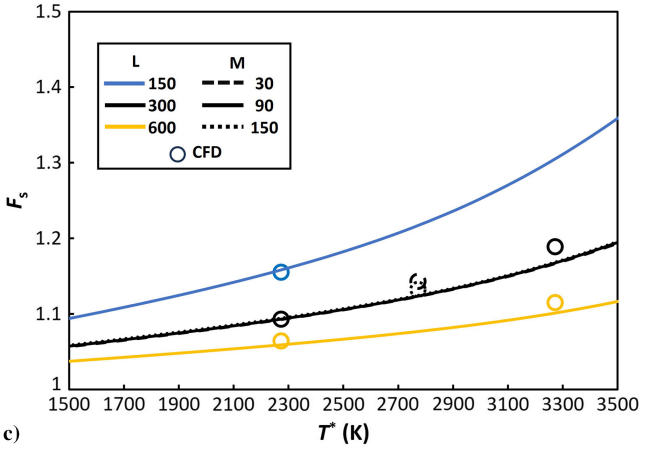

Fig. 11 Predicted F_s as a function of the a) latent heat of evaporation, b) molar mass, and c) T^*.

Fig. 6. However, the numerator of F_s is proportional to $T^*/(1-T^*)$ as given by Eq. (26). Because the magnitude of T_{eq} grows faster than T_s as T^* increases, the margin of safety increases. From these relationships, coolant material with low latent heat and high T^* is preferable to reduce the risk of nucleation of vapor bubbles within the porous leading edge.

From the viewpoint of leading edge engineering, it may be desirable to reduce the peak temperature to avoid thermomechanical failures, to reduce the evaporative heat flux to decrease the cost and weight of the coolant, and to increase F_s to reduce the risk of surface drying out. However, the rather complex relationships presented above do not lend themselves readily to an optimal set of material properties that satisfies all three requirements. For example, TPS utilizing a coolant with a lower T^* would achieve a low operating surface temperature of the TPS, but also result in a low F_s. TPS utilizing a coolant with a higher latent heat of evaporation would achieve a lower evaporative flux but also a lower F_s.

B. Flight Condition

One additional set of parameters one must account for in selecting a coolant material is the vehicle's flight trajectory. We assess a range of flight conditions to examine their effects on the performance of the TPS and thereby guide the selection of the coolant properties. We consider flight altitudes from 20 to 40 km and Mach numbers from 10 to 20. We chose these ranges to emulate the flight trajectories of typical hypersonic vehicles. Figure 12 shows the altitudes and Mach numbers of typical hypersonic flight trajectories and the ranges that we considered. The range within the dashed rectangle is studied using the boundary-layer model and the discrete conditions shown in symbols using DNS.

In Fig. 13 we show the surface temperature, evaporative mass flux, and F_s as a function of the altitude and Mach number to elucidate the relationship among them. The solid lines illustrate the boundary-layer model results, and the symbols represent the DNS results. We consider a leading edge with a fixed radius of 3.1 mm. From our results presented in the previous section, we note that the predicted evaporative flux showed the largest differences between the two models. We therefore consider material D, which has the lowest specific latent heat among the seven materials, to help compare the two models for a wide range of evaporative mass fluxes at the surface. The maximum difference between the two models is below 5% for the surface temperature and F_s and below 25% for the evaporative mass flux.

At high Mach numbers, the severity of the aerothermal conditions is exacerbated due to the high stagnation enthalpy of the hypersonic flows. Figure 13 indeed shows a higher surface temperature, a higher evaporative mass flux, and a lower F_s as the Mach number increases. A higher Mach number significantly increases the incident heat flux,

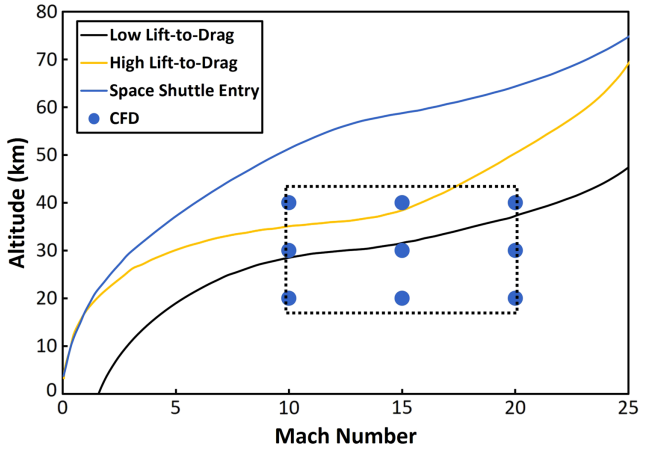

Fig. 12 The velocity–altitude map showing the trajectories of typical hypersonic vehicles and a range of flight conditions used in this study. Data adapted from [44].

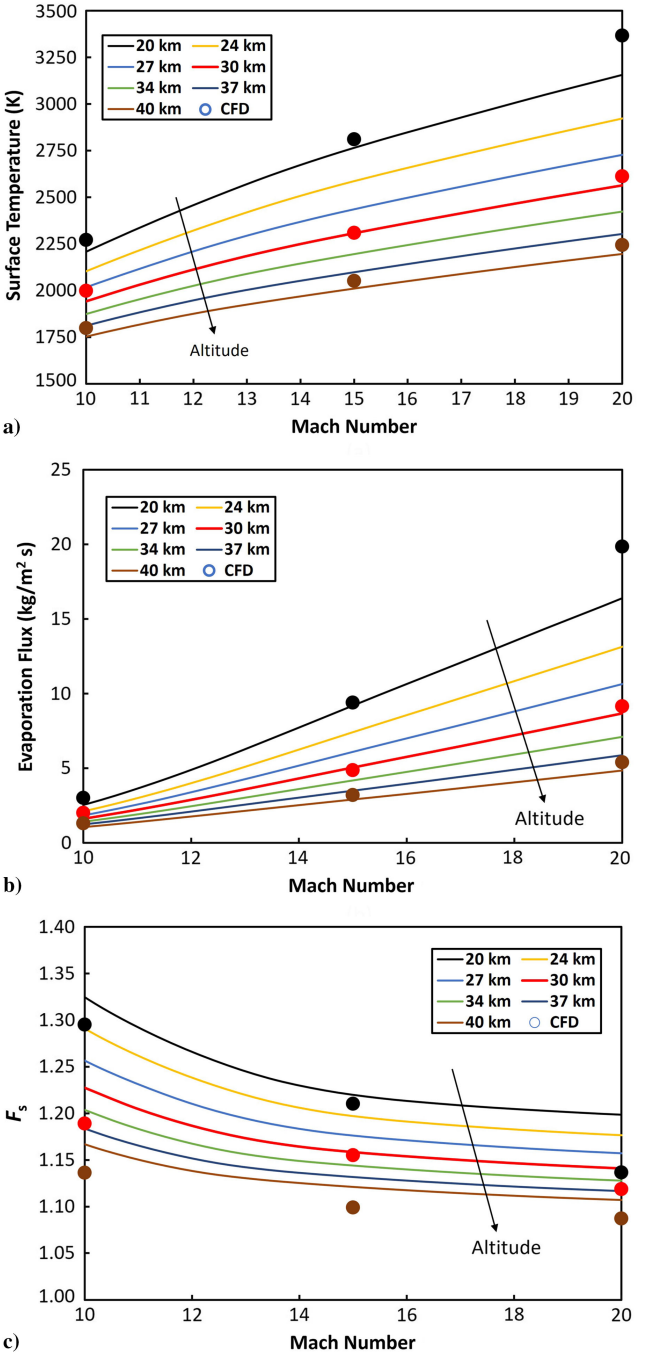

Fig. 13 Predicted a) surface temperature, b) evaporative mass flux, and c) F_s as a function of altitude and Mach number.

which correspondingly requires an increase in the evaporative mass flux to absorb the excess energy. As a result, the surface temperature increases, approaching T_{eq} and thereby decreasing F_s. We note, however, that the changes in the evaporation rate are significantly higher than the changes in the other two parameters. For the range of Mach numbers illustrated in Fig. 13, the evaporative mass flux changes by an order of magnitude, whereas the surface temperature changes less than 50% due to the exponential relationship, as given in Eqs. (18) and (19). F_s experiences an even smaller change of less than 15% due to increases in both the surface temperature and T_{eq} at higher Mach numbers. Therefore, for vehicle trajectories with high Mach numbers, coolant materials with high specific latent heats can significantly reduce the evaporative mass flux. A higher specific latent heat would decrease F_s; however, the reduction in F_s may be acceptable since the decrease in F_s at higher Mach numbers is relatively small.

Conversely, an increase in the flight altitude partly alleviates the severity of the aerothermal condition due to lower densities. Figure 13 shows a decrease in the surface temperature and evaporative mass flux at higher altitudes. However, F_s decreases with increasing altitudes. This is because, at higher altitudes, the stagnation pressure is lower, which reduces the T_{eq} of the coolant. Similar to the results from varying Mach numbers, the evaporative mass flux changes significantly (by a factor of 3) compared to that in the temperature, which varies less than 50%. F_s again experiences a smaller change below 15% due to decreases in both the surface temperature and T_{eq} at higher altitudes. Because the relationship between F_s and the flight altitude is opposite of those for the surface temperature and the evaporative mass flux, different material properties would need to get more emphasis at different altitudes. For instance, a vehicle designed for high-altitude flight may utilize coolants with low specific latent heats and high T^* to increase F_s at the expense of higher surface temperatures and evaporative mass fluxes. Alternatively, a vehicle designed for low-altitude flights may utilize coolants with high latent heat and low T^* to decrease the surface temperature and evaporative mass flux at the expense of lower F_s, which is already relatively high at low altitudes.

C. Leading Edge Radii

Another parameter one must account for in selecting a coolant material is the leading edge radius. Sharp leading edges are essential in achieving superior aerodynamic performance and maneuverability. However, a linear decrease in the leading edge radius linearly increases the squared rate of aerothermal heating [1], which can drastically change the performance of the TPS. Hence, we assess the performance of transpiration-cooling TPS for sharp leading edges with radii from 5 to 0.1 mm and illustrate their impact on the surface temperature, evaporative mass flux, and F_s. We fix the flight condition at 30 km altitude and Mach 15 and use material D.

Figure 14 illustrates the relationship between the leading edge radius and the three performance parameters. Due to a significant increase in the incident heat flux, sharper leading edges exacerbate the aerothermal heating. As a result, the surface temperature and the evaporative mass flux increase while F_s decreases. However, similar to the results in Sec. III.B, the change in the evaporative mass flux is much greater compared with those in the surface temperature and F_s. Reducing the leading edge radius from 5 mm to 0.1 mm, the evaporation rate increases by a factor of 10, while the changes in the surface temperature and F_s are below 4%. This behavior is again due to the nonlinear relationship between the surface temperature and the evaporative mass flux as given by Eqs. (18) and (19). However, the changes in the surface temperature and F_s are much less compared with the results in Sec. III.B because the change in the leading edge radius does not significantly affect the post-shock flow conditions at the stagnation point. Because the change in surface temperature and F_s are almost negligible, the evaporative mass flux is the limiting factor of the TPS for very sharp leading edges. Hence, coolant materials with high specific latent heats would significantly reduce the evaporative mass flux at the expense of marginally higher surface temperature and F_s. We also note that evaporative transpiration cooling may be able to effectively protect very sharp leading edges with a radius of 0.1 mm as long as the necessary evaporative mass flux is achieved at the surface.

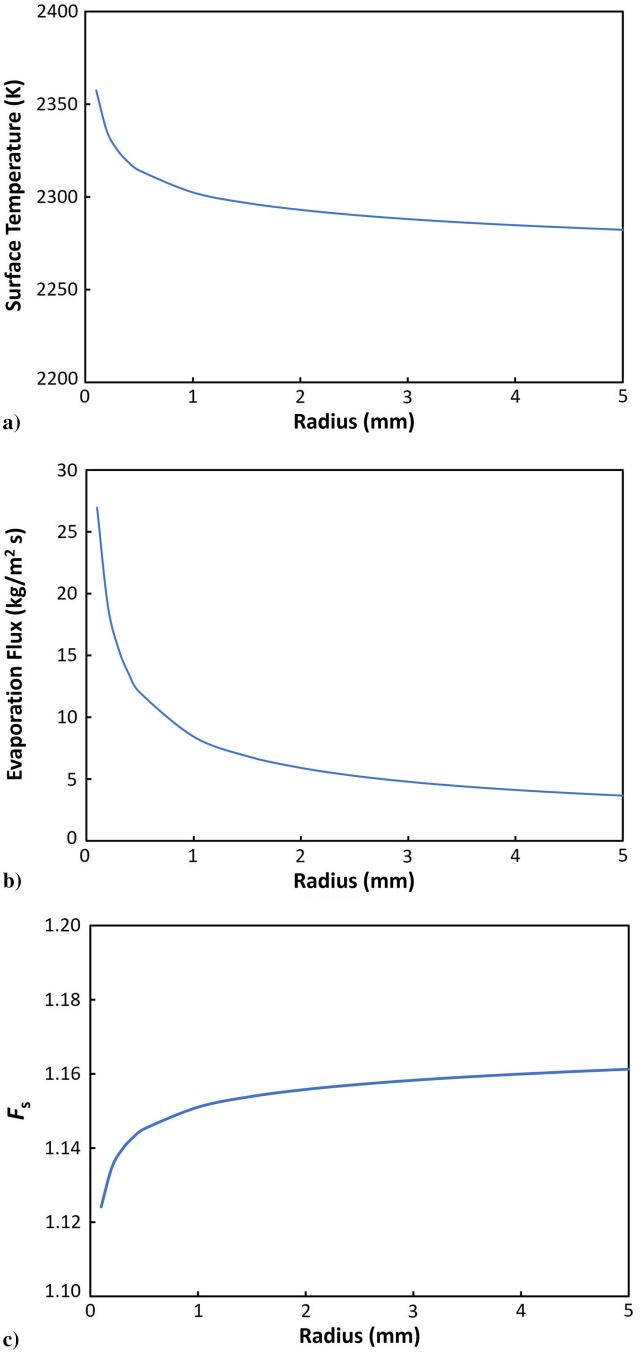

Fig. 14 Predicted a) surface temperature, b) evaporative mass flux, and c) F_s as a function of leading edge radius for edge radius.

IV. Chemical Interaction of Evaporated Vapor

At elevated temperatures, oxide vapors readily dissociate into their elemental constituents. This dissociation reduces the concentration of oxide vapor in the boundary layer, potentially enhancing the rate of evaporation at the surface. Additionally, these dissociation reactions are endothermic, which could further lower the boundary-layer temperature and alleviate the thermal gradient at the surface. This dual effect has the potential to enhance the effectiveness of the evaporative TPS. Here, we incorporate the dissociation of BaO and SiO_2 in our DNS model described in Sec. II to elucidate the effect of oxide dissociation on the evaporation process. The results in this section are obtained at a Mach number of 15 and an altitude of 30 km for a leading edge size of 3.1 mm.

Figure 15 illustrates the surface temperature, evaporation rate, and F_s for SiO_2 and BaO at the stagnation point with different rates of chemical reaction with the hypersonic flow. We find that all three parameters are nearly identical, even if chemical reactions between the oxide vapor and hypersonic flow are incorporated. Figure 16 shows the mass fraction contours near the stagnation point for SiO_2 and BaO coolants. The left-most boundary of the contour is immediately behind the shock, and the right-most boundary of the contour is the leading edge surface. As such, X is the distance from the shock, and Y is the distance from the stagnation line. Despite the high concentrations near the surface and the high temperatures in the flow, almost no dissociation of SiO_2 and BaO occurs, as shown in Fig. 16, to influence the evaporation process. We hypothesize that the significantly low equilibrium constant of oxide vapors inhibits dissociation near the surface due to the relatively low temperature. The temperatures are sufficiently high to promote dissociation of the

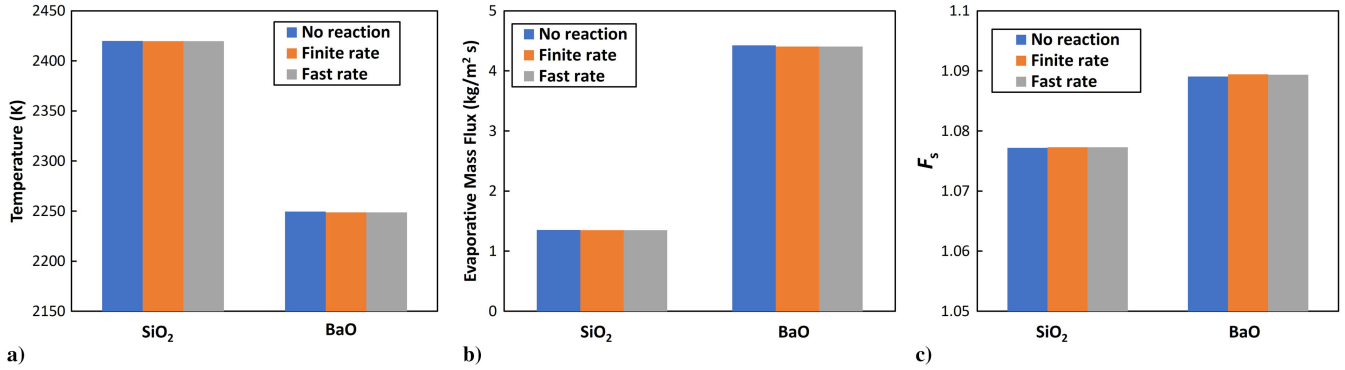

Fig. 15 Predicted a) surface temperature, b) evaporative mass flux, and c) F_s for SiO_2 and BaO coolants with different rates of chemical reaction.

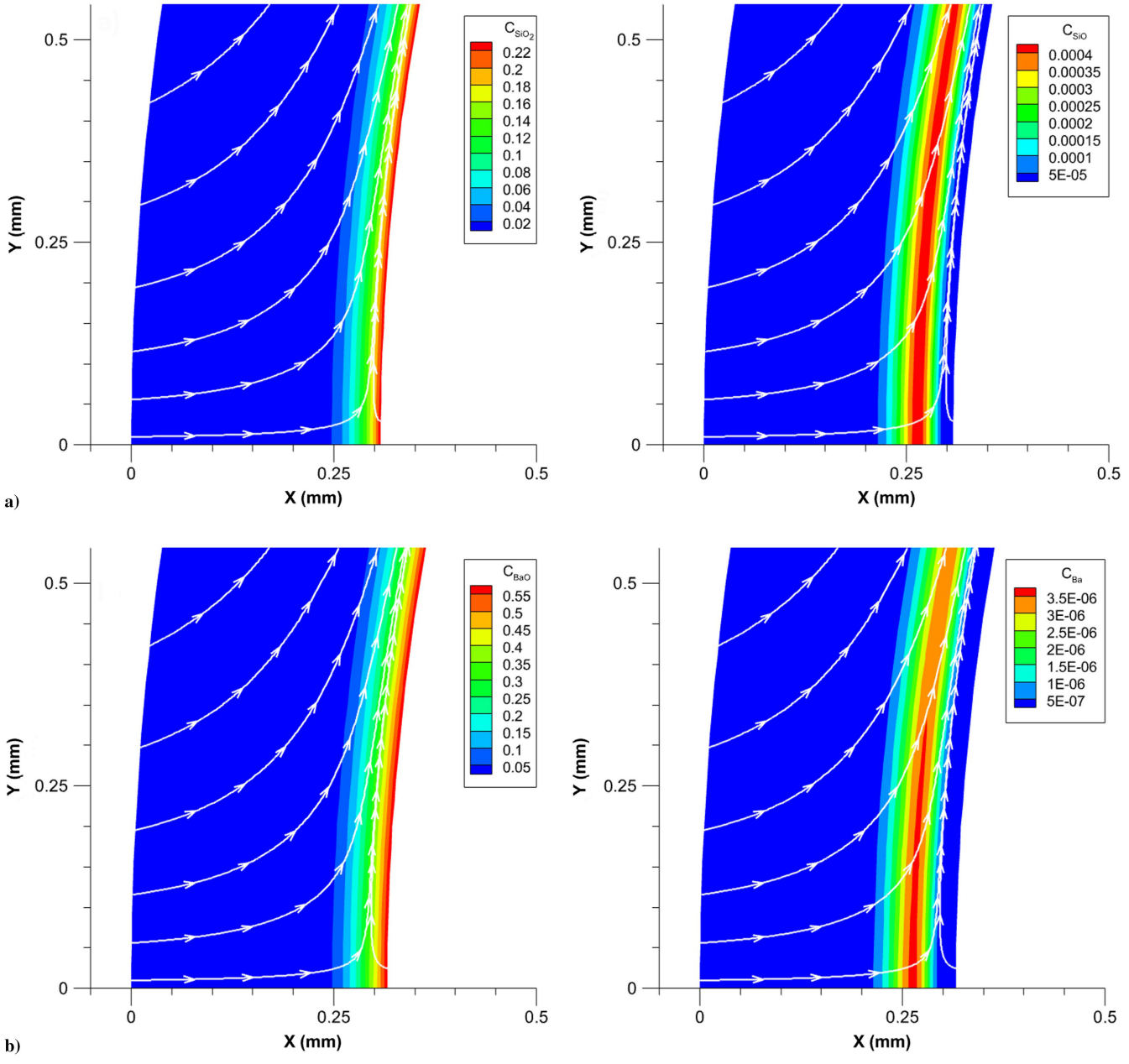

Fig. 16 Mass fraction color contours of a) SiO_2 and b) BaO and their dissociates near the leading edge, with streamlines shown in white lines.

oxide vapor at the edge of the boundary layer. However, we believe that the lack of oxide vapor concentration near the edge of the boundary layer prevents significant dissociation of the oxide vapors. A relatively large concentration of atomic oxygen throughout the boundary layer also inhibits the dissociation of the oxide vapors. Further insights into the dissociation of oxide vapors can be seen in Fig. 17, which shows the magnitudes of the equilibrium constant and mass fraction for atomic oxygen, SiO_2, and BaO as a function of

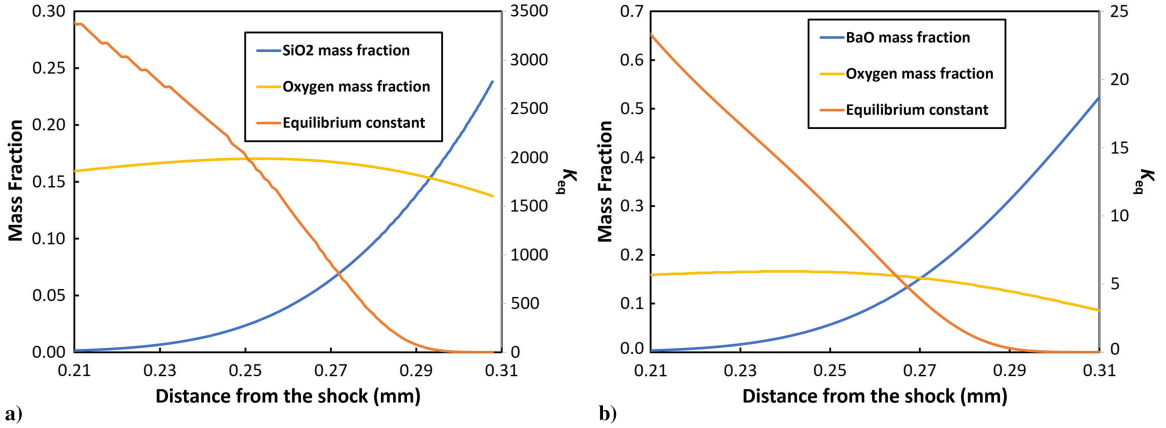

Fig. 17 Mass fractions and equilibrium constants for O and a) SiO_2 and b) BaO as a function of distance away from the surface at the stagnation point.

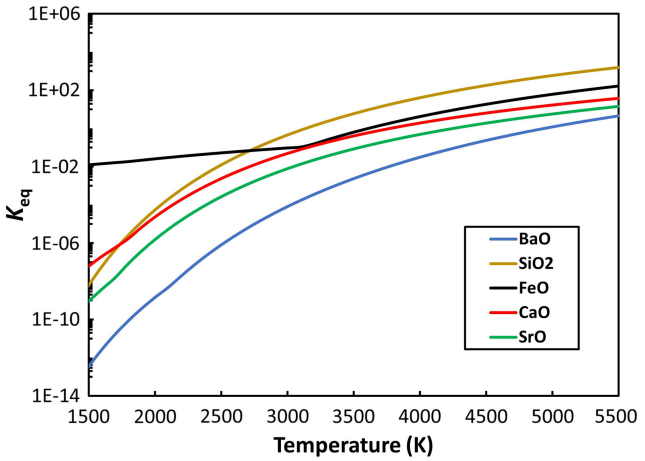

Fig. 18 Equilibrium constants of typical oxides, including BaO and SiO_2, as a function of temperature.

distance from the shock along the stagnation line. The stagnation point is located at the right-most bound of the x axis in Fig. 17. Qualitatively, the location at which the two behaviors that suppress the dissociation of oxide vapors intersect indicates where these effects are minimized. The intersections occur approximately 35 and 50μm from the surface for both BaO and SiO_2, respectively. Thus, the mass fraction of the dissociated oxide vapor reaches its maximum at these locations, as shown in Fig. 16.

Our results suggest that the magnitude of the equilibrium constant and the oxide vapor concentration within the boundary layer predominate the behavior of dissociation, and BaO and SiO_2 both exhibit chemically frozen behavior. Figure 18 shows the equilibrium constants as a function of temperature for various oxides, including BaO and SiO_2. Values for K_{eq} are obtained using the Gibbs free energy of formation of the corresponding oxides obtained from NIST-JANAF thermodynamic table [61]. We emphasize that the equilibrium constants of other typical oxides are similar to those for BaO and SiO_2. Hence, we postulate that other typical oxides also behave chemically frozen with the hypersonic flow and that the frozen flow assumption between the evaporating oxide vapor and the air species is sufficient to accurately characterize the evaporation behavior for transpiration-cooling TPS.

V. Conclusions

In this study, we demonstrated the viability of transpiration cooling employing oxide coolants as a new alternative system to thermally protect sharp leading edges. We parametrically characterize the performance of transpiration cooling for various coolant properties, flight conditions, and leading edge radii using a 2D axisymmetric, semi-analytic boundary-layer model incorporating thermodynamic nonequilibrium conditions, which we validated with third-order shock-fitting DNS. We quantified the performance of the TPS using three metrics: the surface temperature, the evaporative mass flux, and the boiling limit. We showed that, for fixed flight conditions and leading edge sizes, the surface temperature depends mainly on the saturation temperature of the coolant material, the boiling limit is largely independent of molar mass, and the evaporative mass flux is affected by all three material properties. We also illustrated that high Mach numbers and small leading edge sizes exacerbate the aerothermal condition, resulting in a higher surface temperature and evaporative mass flux and a lower boiling limit factor of safety. Low-altitude flights also increase the surface temperature and evaporative mass flux but result in a higher boiling limit factor of safety. We further utilized third-order shock-fitting DNS to demonstrate that oxide vapors exhibit chemically frozen behavior within the boundary layer due to their chemical inertness near the surface and their low concentrations near the edge of the boundary layer. Comparisons between the boundary-layer model and the DNS solutions showed less than 5% difference in surface temperature at the stagnation point. The sources of discrepancy between the two models were discussed and explained to result from the high mass fraction of evaporating species at the stagnation point and the fully catalytic boundary condition used by the boundary-layer model. The low and explainable discrepancies between the two different solution methods show successful validation of both methods.

Our numerical results demonstrated that transpiration cooling employing oxide coolants may effectively cool the surface temperature to below the saturation temperature of the coolant material. As long as the necessary amount of coolant is supplied to the surface, transpiration cooling can effectively cool even for very sharp leading edges with a radius of 0.1 mm and in extreme hypersonic conditions as high as Mach 20 and as low as 20 km altitude, where incident heat fluxes are of the order of 85 MW/m^2. Our results do not lend themselves readily to a single optimal set of the material properties for transpiration cooling. Rather, different coolant properties are better suited for different flight conditions and leading edge sizes. Vehicles with high Mach numbers and low-altitude trajectories or small radius of curvature of the leading edge may utilize coolant materials with high specific latent heats to significantly reduce the evaporative mass flux. Alternatively, vehicles with high-altitude trajectories may benefit from coolants with low specific latent heats to avoid vapor nucleation within the porous leading edge, to which they are more susceptible at higher altitudes. These results offer proof of the viability of a novel method of thermally protecting sharp leading edges in various extreme hypersonic flight environments.

Acknowledgments

We would like to thank ACCESS program management and the teams responsible for maintaining the TACC Stampede2 and Purdue Anvil advanced computing centers.

References

[1] Van Driest, E. R., "The Problem of Aerodynamic Heating," *Aeronautical Engineering Review*, Vol. 15, No. 10, 1956, pp. 26–41.

[2] Fay, J. A., and Riddell, F. R., "Theory of Stagnation Point Heat Transfer in Dissociated Air," *Journal of the Aerospace Sciences*, Vol. 25, No. 2, 1958, pp. 73–85. https://doi.org/10.2514/8.7517

[3] Miller, I. M., and Sutton, K., "An Experimental Study of the Oxidation of Graphite in High-Temperature Supersonic and Hypersonic Environments," NASA TN-D-3444, July 1966.

[4] Lundell, J. H., and Dickey, R. R., "Ablation of ATJ Graphite at High Temperatures," *AIAA Journal*, Vol. 11, No. 2, 1973, pp. 216–222. https://doi.org/10.2514/3.50451

[5] Yan, X., Huang, H., Fan, Z., Hong, C., and Hu, P., "Assessment of a 3D Ablation Material Response Model for Lightweight Quartz Fiber Reinforced Phenolic Composite," *Polymer Composites*, Vol. 43, No. 11, 2022, pp. 8341–8355. https://doi.org/10.1002/pc.27005

[6] Tran, H., Johnson, C., Rasky, D., Hui, F., Hsu, M.-T., and Chen, Y., "Phenolic Impregnated Carbon Ablators (PICA) for Discovery Class Missions," *31st Thermophysics Conference*, AIAA Paper 1996-1911, 1996. https://doi.org/10.2514/6.1996-1911

[7] Meurisse, J. B. E., Chatzigeorgis, G. B., Diaz, P. V., Bessire, B. K., Panerai, F., and Mansour, N. N., "Equilibrium Model for the Ablation Response of Silicone-Coated PICA," *International Journal of Heat and Mass Transfer*, Vol. 201, Feb. 2023, Paper 123523, https://doi.org/10.1016/j.ijheatmasstransfer.2022.123523

[8] Zhu, Y., Peng, W., Xu, R., and Jiang, P., "Review on Active Thermal Protection and Its Heat Transfer for Airbreathing Hypersonic Vehicles," *Chinese Journal of Aeronautics*, Vol. 31, No. 10, 2018, pp. 1929–1953. https://doi.org/10.1016/j.cja.2018.06.011

[9] Zhang, S., Li, X., Zuo, J., Qin, J., Cheng, K., Feng, Y., and Bao, W., "Research Progress on Active Thermal Protection for Hypersonic Vehicles," *Progress in Aerospace Sciences*, Vol. 119, Nov. 2020, Paper 100646. https://doi.org/10.1016/j.paerosci.2020.100646

[10] Hanquist, K. M., Hara, K., and Boyd, I. D., "Detailed Modeling of Electron Emission for Transpiration Cooling of Hypersonic Vehicles," *Journal of Applied Physics*, Vol. 121, No. 5, 2017, Paper 053302. https://doi.org/10.1063/1.4974961

[11] Campbell, N. S., Hanquist, K., Morin, A., Meyers, J., and Boyd, I., "Evaluation of Computational Models for Electron Transpiration Cooling," *Aerospace*, Vol. 8, No. 9, 2021, p. 243. https://doi.org/10.3390/aerospace8090243

[12] Sahu, R., Tropina, A., Andrienko, D., and Miles, R., "Cesium Seeding for Effective Electron Transpiration Cooling in Hypersonic Flows," *Plasma Sources Science and Technology*, Vol. 31, No. 3, 2022, Paper 035001. https://doi.org/10.1088/1361-6595/ac4ecc

[13] Weston, K. C., "The Stagnation-Point Boundary Layer with Suction and Injection in Equilibrium Dissociating Air," NASA TN-D-3889, Dec. 1968.

[14] Henline, W. D., "Transpiration Cooling of Hypersonic Blunt Bodies with Finite Rate Surface Reactions," NASA TR-A-89018, Feb. 1989.

[15] Otsu, H., Fujita, K., and Ito, T., "Application of the Transpiration Cooling Method for Reentry Vehicles," *45th AIAA Aerospace Sciences Meeting and Exhibit*, AIAA Paper 2007-1209, 2007. https://doi.org/10.2514/6.2007-1209

[16] Jiang, P.-X., Huang, G., Zhu, Y., Liao, Z., and Huang, Z., "Experimental Investigation of Combined Transpiration and Film Cooling for Sintered Metal Porous Struts," *International Journal of Heat and Mass Transfer*, Vol. 108, May 2017, pp. 232–243. https://doi.org/10.1016/j.ijheatmasstransfer.2016.12.014

[17] Wu, N., Wang, J., He, F., Chen, L., and Ai, B., "Optimization Transpiration Cooling of Nose Cone with Non-Uniform Permeability," *International Journal of Heat and Mass Transfer*, Vol. 127, Dec. 2018, pp. 882–891. https://doi.org/10.1016/j.ijheatmasstransfer.2018.07.134

[18] Gulli, S., and Maddalena, L., "Arc-Jet Testing of a Variable-Transpiration-Cooled and Uncoated Carbon-Carbon Nose Cone," *Journal of Spacecraft and Rockets*, Vol. 56, No. 3, 2019, pp. 780–788. https://doi.org/10.2514/1.A34176

[19] He, F., Wu, N., Ran, F., and Wang, J., "Numerical Investigation on the Transpiration Cooling of Three-Dimensional Hypersonic Inlet," *Aerospace Science and Technology*, Vol. 106, Nov. 2020, Paper 106152, https://doi.org/10.1016/j.ast.2020.106152

[20] Ifti, H. S., Hermann, T., McGilvray, M., and Merrifield, J., "Numerical Simulation of Transpiration Cooling in a Laminar Hypersonic Boundary Layer," *Journal of Spacecraft and Rockets*, Vol. 59, No. 5, 2022, pp. 1726–1735. https://doi.org/10.2514/1.A35325

[21] Ewenz Rocher, M., Hermann, T., McGilvray, M., and Gollan, R., "Correlation for Species Concentration on a Hypersonic Stagnation Point with Mass Injection," *AIAA Journal*, Vol. 60, No. 5, 2022, pp. 2798–2809. https://doi.org/10.2514/1.J061159

[22] Van Foreest, A., Sippel, M., Gülhan, A., Esser, B., Ambrosius, B. A. C., and Sudmeijer, K., "Transpiration Cooling Using Liquid Water," *Journal of Thermophysics and Heat Transfer*, Vol. 23, No. 4, 2009, pp. 693–702. https://doi.org/10.2514/1.39070

[23] Reimer, T., Kuhn, M., Gülhan, A., Esser, B., Sippel, M., and van Foreest, A., "Transpiration Cooling Tests of Porous CMC in Hypersonic Flow," *17th AIAA International Space Planes and Hypersonic Systems and Technologies Conference*, AIAA Paper 2011-2251, 2011. https://doi.org/10.2514/6.2011-2251

[24] Wang, J., Zhao, L., Wang, X., Ma, J., and Lin, J., "An Experimental Investigation on Transpiration Cooling of Wedge Shaped Nose Cone with Liquid Coolant," *International Journal of Heat and Mass Transfer*, Vol. 75, Aug. 2014, pp. 442–449. https://doi.org/10.1016/j.ijheatmasstransfer.2014.03.076

[25] He, F., and Wang, J., "Numerical Investigation on Critical Heat Flux and Coolant Volume Required for Transpiration Cooling with Phase Change," *Energy Conversion and Management*, Vol. 80, April 2014, pp. 591–597. https://doi.org/10.1016/j.enconman.2014.02.003

[26] Shen, L., Wang, J., Dong, W., Pu, J., Peng, J., Qu, D., and Chen, L., "An Experimental Investigation on Transpiration Cooling with Phase Change under Supersonic Condition," *Applied Thermal Engineering*, Vol. 105, July 2016, pp. 549–556. https://doi.org/10.1016/j.applthermaleng.2016.03.039

[27] Huang, G., Zhu, Y., Liao, Z., and Jiang, P.-X., "Experimental Investigation of Self-Pumping Internal Transpiration Cooling," *International Journal of Heat and Mass Transfer*, Vol. 123, Aug. 2018, pp. 514–522. https://doi.org/10.1016/j.ijheatmasstransfer.2018.02.046

[28] Huang, G., Liao, Z., Xu, R., Zhu, Y., and Jiang, P.-X., "Self-Pumping Transpiration Cooling with a Protective Porous Armor," *Applied Thermal Engineering*, Vol. 164, Jan. 2020, Paper 114485. https://doi.org/10.1016/j.applthermaleng.2019.114485

[29] Bethe, H. A., and Adams, M. C., "A Theory for the Ablation of Glassy Materials," *Journal of the Aerospace Sciences*, Vol. 26, No. 6, 1959, pp. 321–328. https://doi.org/10.2514/8.8080

[30] Hidalgo, H., "Ablation of Glassy Material Around Blunt Bodies of Revolution," *ARS Journal*, Vol. 30, No. 9, 1960, pp. 806–814. https://doi.org/10.2514/8.5240

[31] Roberts, L., "Stagnation-Point Shielding by Melting and Vaporization," NASA TR-R-10, Jan. 1959.

[32] Chen, Y.-K., Stern, E. C., and Agrawal, P., "Thermal Ablation Simulations of Quartz Materials," *Journal of Spacecraft and Rockets*, Vol. 56, No. 3, 2019, pp. 865–874. https://doi.org/10.2514/1.A34303

[33] Su, H., Wang, J., He, F., Chen, L., and Ai, B., "Numerical Investigation on Transpiration Cooling with Coolant Phase Change under Hypersonic Conditions," *International Journal of Heat and Mass Transfer*, Vol. 129, Feb. 2019, pp. 480–490. https://doi.org/10.1016/j.ijheatmasstransfer.2018.09.123

[34] Su, H., He, F., Wang, J., Luo, X., and Ai, B., "Numerical Investigation on the Effects of Porous Cone Parameters on Liquid Transpiration Cooling Performance," *International Journal of Thermal Sciences*, Vol. 161, March 2021, Paper 106743. https://doi.org/10.1016/j.ijthermalsci.2020.106743

[35] Scala, S. M., and Vidale, G. L., "Vaporization Processes in the Hypersonic Laminar Boundary Layer," *International Journal of Heat and Mass Transfer*, Vol. 1, No. 1, 1960, pp. 4–22. https://doi.org/10.1016/0017-9310(60)90003-X

[36] Charwat, A. F., "The Effect of Surface-Evaporation Kinetics On Sublimation Near the Leading Edge," *International Journal of Heat and Mass Transfer*, Vol. 8, No. 3, 1965, pp. 383–394. https://doi.org/10.1016/0017-9310(65)90001-3

[37] Kubota, T., "Ablation With Ice Model at M = 5.8," *ARS Journal*, Vol. 30, No. 12, 1960, pp. 1164–1169. https://doi.org/10.2514/8.5355

[38] Baker, R. L., "Graphite Sublimation Chemistry Nonequilibrium Effects," *AIAA Journal*, Vol. 15, No. 10, 1977, pp. 1391–1397. https://doi.org/10.2514/3.60806

[39] Faghri, A., "Heat Transfer Limitations," *Heat Pipe Science and Technology*, Taylor & Francis, New York, 1995, pp. 221–267.
[40] Mortensen, C. H., and Zhong, X., "Simulation of Second-Mode Instability in a Real-Gas Hypersonic Flow with Graphite Ablation," *AIAA Journal*, Vol. 52, No. 8, 2014, pp. 1632–1652. https://doi.org/10.2514/1.J052659
[41] Mortensen, C. H., and Zhong, X., "Real-Gas and Surface-Ablation Effects on Hypersonic Boundary-Layer Instability over a Blunt Cone," *AIAA Journal*, Vol. 54, No. 3, 2016, pp. 980–998. https://doi.org/10.2514/1.J054404
[42] Dias, B., Turchi, A., Stern, E. C., and Magin, T. E., "A Model for Meteoroid Ablation Including Melting and Vaporization," *Icarus*, Vol. 345, July 2020, Paper 113710. https://doi.org/10.1016/j.icarus.2020.113710
[43] Raghunandan, P., Haskins, J. B., Palmer, G. E., Bessire, B. K., and Stern, E. C., "Material Response Modeling of Melt Flow-Vapor Ablation for Iron," *AIAA Journal*, Vol. 60, No. 4, 2022, pp. 2028–2038. https://doi.org/10.2514/1.J060788
[44] Anderson, J. D., Jr., *Hypersonic and High-Temperature Gas Dynamics*, AIAA, Reston, VA, 2019.
[45] Hirschfelder, J. O., Curtiss, C. F., and Bird, R. B., *The Molecular Theory of Gases and Liquids*, Wiley, New York, 1954.
[46] Wittliff, C. E., and Curtis, J. T., "Normal Shock Wave Parameters in Equilibrium Air," Rept. CAL-111 (Contract No. AF 33 (616)-6579), Cornell Aeronaut. Lab., Nov. 1961. https://doi.org/10.21236/AD0270202
[47] Bejan, A., "Laminar Boundary Layer Flow," *Convection Heat Transfer*, Wiley, Hoboken, NJ, 2013, pp. 30–96.
[48] Ma, Y., and Zhong, X., "Numerical Simulation of Receptivity and Stability of Nonequilibrium Reacting Hypersonic Boundary Layers," *AIAA 39th Aerospace Sconces Meeting and Exhibit*, AIAA Paper 2001-0892, 2001. https://doi.org/10.2514/6.2001-892
[49] Mortensen, C. H., "Effects of Thermochemical Nonequilibrium on Hypersonic Boundary-Layer Instability in the Presence of Surface Ablation or Isolated Two-Dimensional Roughness," Ph.D. Dissertation, Univ. of California, Los Angeles, 2015.
[50] Park, C., *Nonequilibrium Hypersonic Aerothermodynamics*, Wiley, New York, 1990.
[51] Lee, J.-H., "Basic Governing Equations for the Flight Regimes of Aeroassisted Orbital Transfer Vehicles," *19th Thermophysics Conference*, Vol. 96, AIAA, New York, June 1984, pp. 3–53; also AIAA Paper 1984-1729; Seen in Thermal Design of Aeroassisted Orbital Transfer Vehicles, edited by Nelson, HF. https://doi.org/10.2514/6.1984-1729
[52] Blottner, F. G., Johnson, M., and Ellis, M., "Chemically Reacting Viscous Flow Program for Multi-Component Gas Mixtures," Tech. Rept. SC-RR-70-754, Sandia Lab., Albuquerque, NM, Jan. 1971. https://doi.org/10.2172/4658539
[53] Gupta, R., Lee, K.-P., Moos, J., and Sutton, K., "Viscous-Shock-Layer Solutions with Coupled Radiation and Ablation Injection for Earth Entry," *5th Joint Thermophysics and Heat Transfer Conference*, AIAA Paper 1990-1697, 1990. https://doi.org/10.2514/6.1990-1697
[54] Breck, D. W., and Breck, D. W., *Zeolite Molecular Sieves: Structure, Chemistry, and Use*, Wiley, New York, 1973, p. 636.
[55] Wilke, C. R., "A Viscosity Equation for Gas Mixtures," *Journal of Chemical Physics*, Vol. 18, No. 4, 1950, pp. 517–519. https://doi.org/10.1063/1.1747673
[56] Haynes, W. M., *CRC Handbook of Chemistry and Physics*, CRC Press, Boca Raton, FL, 2016.
[57] Park, C., "On Convergence of Computation of Chemically Reacting Flows," AIAA Paper 1985-0247, 1985. https://doi.org/10.2514/6.1985-247
[58] Bhutta, B. A., and Lewis, C. H., "Low-to-High Altitude Predictions of Three-Dimensional Ablative Re-Entry Flowfields," *Journal of Spacecraft and Rockets*, Vol. 30, No. 4, 1993, pp. 395–403. https://doi.org/10.2514/3.25544
[59] Park, C., Howe, J., Jaffe, R., and Candler, G., "Chemical-Kinetic Problems of Future NASA Missions," *29th Aerospace Sciences Meeting*, AIAA Paper 1991-0464, 1991. https://doi.org/10.2514/6.1991-464
[60] McBride, B. J., "Thermodynamic Properties to 6000 K for 210 Substances Involving the First 18 Elements," NASA SP-3001, Office of Scientific and Technical Information, 1963.
[61] Malcolm, W., and Chase, J., "NIST-JANAF Thermochemical Tables," *Journal of Physical and Chemical Reference Data*, Vol. 14, 1985, pp. 1–1856.
[62] Dickstein, D. A., "Reticulated Foam Materials for the Evaporative Cooling of Hypersonic Vehicles & for Control of Secondary Electron Emission in Space Electric Propulsion," Ph.D. Dissertation, Univ. of California, Los Angeles, 2022.
[63] Shishkin, R., and Yuferov, Y., "Fabrication of SiC Matrix Composite Material by Pressureless Aluminum Melt Infiltration in Air Atmosphere," *Composites Communications*, Vol. 32, June 2022, Paper 101176. https://doi.org/10.1016/j.coco.2022.101176
[64] Johnston, C. O., "Influence of Coupled Radiation and Ablation on Meteor Entries," *47th AIAA Thermophysics Conference*, AIAA paper 2017-4533, 2017. https://doi.org/10.2514/6.2017-4533